Princeton Plasma Physics Laboratory

PPPL- 4365

PPPL- 4365

Two-dimensional Fully Kinetic Simulations Of Driven Magnetic Reconnection With Boundary Conditions Relevant To The Magnetic Reconnection Experiment

S. Dorfman, W. Daughton, V. Roytershteyn, H. Ji, Y. Ren, and M. Yamada

November, 2008

PPPL PRINCETON PLASMA PHYSICS LABORATORY

Prepared for the U.S. Department of Energy under Contract DE-AC02-76CH03073.

Princeton Plasma Physics Laboratory
Report Disclaimers

Full Legal Disclaimer

Trademark Disclaimer

PPPL Report Availability

Princeton Plasma Physics Laboratory:

http://www.pppl.gov/techreports.cfm

Office of Scientific and Technical Information (OSTI):

http://www.osti.gov/bridge

Related Links:

U.S. Department of Energy

Office of Scientific and Technical Information

Fusion Links

Two-dimensional fully kinetic simulations of driven magnetic reconnection with boundary conditions relevant to the Magnetic Reconnection Experiment

S. Dorfman,[1] W. Daughton,[2] V. Roytershteyn,[2] H. Ji,[1] Y. Ren,[3] and M. Yamada[1]
[1]*Center for Magnetic Self-organization in Laboratory and Astrophysical Plasmas, Princeton Plasma Physics Laboratory, Princeton, New Jersey 08543, USA*
[2]*Los Alamos National Laboratory, Los Alamos, New Mexico 87545, USA*
[3]*Center for Magnetic Self-organization in Laboratory and Astrophysical Plasmas, University of Wisconsin, Madison, Wisconsin 53706, USA*

(Received 7 July 2008; accepted 8 September 2008; published online 17 October 2008)

Two-dimensional fully kinetic simulations are performed using global boundary conditions relevant to model the Magnetic Reconnection Experiment (MRX) [M. Yamada *et al.*, Phys Plasmas **4**, 1936 (1997)]. The geometry is scaled in terms of the ion kinetic scales in the experiment, and a reconnection layer is created by reducing the toroidal current in the flux cores in a manner similar to the actual experiment. The ion-scale features in these kinetic simulations are in remarkable agreement with those observed in MRX, including the reconnection inflow rate and quadrupole field structure. In contrast, there are significant discrepancies in the simulated structure of the electron layer that remain unexplained. In particular, the measured thickness of the electron layers is 3–5 times thicker in MRX than in the kinetic simulations. The layer length is highly sensitive to downstream boundary conditions as well as the time over which the simulation is driven. However, for a fixed set of chosen boundary conditions, an extrapolation of the scaling with the ion to electron mass ratio implies that at realistic mass ratio both the length and width will be too small compared to the experiment. This discrepancy implies that the basic electron layer physics may differ significantly between MRX and the two-dimensional, collisionless simulations. The two leading possibilities to explain the discrepancy are weak Coulomb collisions and three-dimensional effects that are present in the experiment but not included in the simulation model. © *2008 American Institute of Physics*. [DOI: 10.1063/1.2991361]

I. INTRODUCTION

Although magnetic reconnection has far-reaching applications in space and laboratory plasmas, many important issues remain unresolved for collisionless regimes. In particular, the basic structure of reconnection layers and the nature of the mechanisms responsible for the observed reconnection rates remain active research topics in theory, simulation, and experiment.[1–3]

Most theoretical work has focused on the limit of two-dimensional (2D) steady-state reconnection where conservation laws imply a direct link between the geometry of the diffusion region and the reconnection rate. Within the context of resistive magnetohydrodynamics (MHD), a variety of solutions are possible depending on the localization scale of the resistivity. Uniform resistivity gives rise to Sweet–Parker solutions with slow reconnection rates, while localized resistivity results in Petschek-type solutions with fast reconnection.[4–6]

In weakly collisional and collisionless regimes, the structure of the diffusion region is significantly more complicated, consisting of an inner electron diffusion region and an outer ion diffusion region. The physics responsible for controlling the length of these layers remains controversial and poorly understood. For anti-parallel reconnection, early kinetic simulations[7,8] predicted a very short electron diffusion region ($\sim 5d_e$), while the length of the ion diffusion region was $\sim 10d_i$. However, new large-scale kinetic simulations have demonstrated that the electron region can form a highly elongated sheet[2] with a two-scale structure[9,10] along the outflow. These elongated electron layers are unstable to secondary-island formation, leading to a time-dependent process.[2,9] Certain features of these new predictions have been seen in recent satellite observations at the magnetopause,[11] but many uncertainties remain. In particular, these new results are at odds with most two-fluid simulations where the aspect ratio of the electron layer remains compact and the reconnection process is steady.[12,13] Nevertheless, recent results from electron MHD suggest that a range of different aspect ratios are in principle possible depending on the dissipation mechanism and boundary conditions.[14]

Until recently, the physics responsible for controlling the thickness of each layer has been less controversial. For anti-parallel reconnection in the collisionless regime, scaling arguments predict a half thickness $\delta_s \sim d_s$ for each layer (where $d_s = c/\omega_{ps}$ and $\omega_{ps} = (4\pi e^2 n/m_s)^{1/2}$, $s = i, e$). Two-dimensional (2D) kinetic simulations are in excellent agreement with this scaling, with the observed half thickness of the electron layer in the range $\delta_e \approx (1-2)d_e$. However, somewhat thicker electron layers have been inferred from satellite observations,[15,16] where $\delta_e \sim (3-5)d_e$, and recent measurements[3,17,18] on the Magnetic Reconnection Experi-

ment (MRX), where $\delta_e \sim 8d_e$. These measurements have important implications for the nature of the dissipation mechanism operative at the X-line. In 2D collisionless models, the off-diagonal portion of the electron pressure tensor is responsible for breaking the frozen-in condition inside the electron layer. This is often referred to as nongyrotropic pressure because these terms arise from a breakdown in the gyrosymmetry within the electron layer. The potential importance of these terms was first identified by Vasyliunas[19] and analyzed in detail by Dungey.[20] Since the magnitude of these off-diagonal terms scales as $\sim(\rho_e/\delta_e)^2$ (where ρ_e is the electron orbit size), the thickness of the electron layer plays a crucial role. Rough estimates from satellite observations indicate the off-diagonal terms may be sufficient to balance the reconnection electric field in the magnetotail.[21] In addition, 2D kinetic simulations[7,22,23] have clearly demonstrated that the nongyrotropic pressure terms play a crucial role in the force balance. Although similar results have been demonstrated in limited three-dimensional (3D) simulations,[24] large-scale 3D simulations with sufficient spatial resolution to allow a full spectrum of current aligned instabilities remain infeasible; thus, there is considerable uncertainty in how these modes may influence the average thickness of the electron layer.

Clearly, there are a number of unresolved questions regarding the basic structure of the electron diffusion region in which controlled laboratory experiments with sufficient diagnostics to resolve the layer could prove extremely valuable. The Magnetic Reconnection Experiment (MRX) is one such experiment that has been used to study the basic physics of magnetic reconnection.[25] Currents in a pair of axisymmetric flux cores create the plasma and drive the reconnection. Typical parameters are $B=100-500$ G, $n_e=10^{13}-10^{14}$ cm^{-3}, and $T_e=1-10$ eV. Scale separation between ions and electrons in the form of the quadrupole field associated with Hall reconnection has been observed and characterized.[26] Calculated in-plane electron flows display similar features to numerical simulations with geometry and boundary conditions different from that of the experiment.[27] Recently improved diagnostics have enabled a 2.5× improved resolution, opening up the possibility of detailed comparisons with simulations[3,17,18] to better understand the structure of the electron layer.

Previous two-fluid simulations of MRX[28] have been shown to well match the global parameters and features of the toroidal geometry. However, this approach neglects kinetic effects that may play a role at the electron layer scale. For example, the electrons within the current layer are expected to undergo a variety of complicated crossing orbits for the configuration typical in most discharges. To first approximation, collisions can be neglected since the typical electron mean free path in MRX ~10 cm is an order of magnitude larger than the thickness of the electron layer ~1 cm. These considerations imply that a fully kinetic particle-in-cell (PIC) simulation is a reasonable first approximation to capture the key reconnection physics in the experiment.

Most kinetic PIC studies employ a Harris sheet equilibrium with simple periodic boundary conditions to examine undriven reconnection where the evolution is determined from the pre-existing gradients within the initial current sheet. This approach is not well suited for making direct comparisons with the driven reconnection process in MRX, where the rate at which flux is driven and the global boundary conditions[29] may play a crucial role in determining the structure of the reconnection layer.

Motivated by these considerations, this work describes 2D fully kinetic PIC simulations using boundary conditions relevant to MRX. Initial comparisons of the electron layer width and structure were reported in a previous publication;[3] this work expands on those results and includes a detailed description of the simulation model, the methodology used to investigate the key physics, and a careful analysis of the simulation results. The basic approach involves matching the box geometry in terms of ion inertial lengths and driving the reconnection dynamics by decreasing the out-of-plane current in the flux cores in the same manner as the actual experiment. For consistency, the electron layer length and width in the simulation are defined the same way as in the experiment: the layer length is the distance from the X-point to the location of the peak electron outflow; the layer width is the half width at 40% maximum of the electron outflow channel at the location of peak electron outflow.[17] Due to computational limitations, it is necessary to employ an artificial ion to electron mass ratio $m_i/m_e=10-150$, but scalings with this parameter are examined to extrapolate the results to physically relevant values. After carefully examining the mass ratio scaling and considering a range of relevant drive times and variation in the downstream boundary conditions, a fundamental discrepancy remains unexplained.[3] Although the simulation results demonstrate a striking resemblance to the observed ion scale features in MRX, the electron layer is 3–5 times thicker in MRX than in the simulations. The layer aspect ratio, while highly sensitive to the downstream boundary conditions, is approximately independent of m_i/m_e for a fixed set of chosen boundary conditions. Extrapolated to a realistic mass ratio, the electron layer in the simulation is thus smaller than that in the experiment. These discrepancies have important implications for the nature of the physical mechanism that balances the reconnecting electric field within the layer and point to the need to consider Coulomb collisions and 3D effects such as current aligned instabilities in future work.

II. THE SIMULATION MODEL

The basic strategy is to choose an appropriate set of boundary conditions to mimic the driven reconnection process in MRX, without being encumbered with too many technical details. Clearly, the actual experiment is considerably more complicated than one can realistically hope to replicate in a kinetic simulation. However, there are good reasons to suspect that many of these details are less relevant to the central motivation of this work—a better understanding of the basic structure of the electron diffusion region. In order to avoid the technical details needed to simulate the actual toroidal geometry of MRX, this effort employs a 2D Cartesian simulation domain as illustrated in Fig. 1. This is a reasonable choice since the influence of toroidicity is prob-

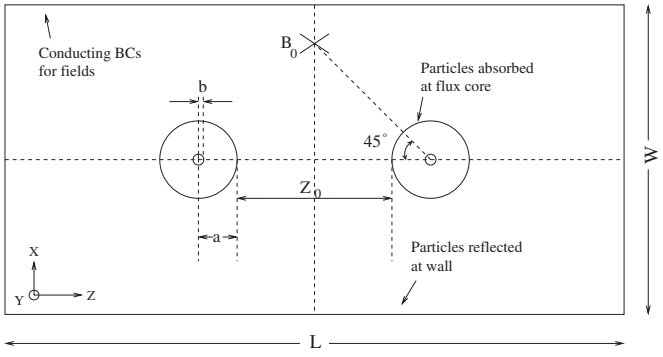

FIG. 1. Basic schematic of simulation domain and boundary conditions employed to mimic the MRX experiment. Computational grid covers the entire rectangular domain. Field boundary conditions are applied only on the outer boundary, while particle boundary conditions are applied at the surface of the flux cores and the outer wall. The current inside the flux cores is prescribed as a function of time. For all simulations presented in this article, $L=150$ cm, $W=75$ cm, $a=9.4$ cm, $b=1.3$ cm, and $Z_0=40$ cm.

ably a second-order effect in regards to basic structure of the electron layer. Furthermore, this choice permits a straight forward implementation of the boundary conditions into virtually any existing PIC code.

A. Code and boundary conditions

For the present study, the boundary conditions were implemented into a parallel PIC code that has been used extensively to model current sheet instabilities[30,31] and magnetic reconnection.[2] In this full-Maxwell approach, the fields are advanced using the scalar and vector potentials. The scalar potential is computed directly from Poisson's equation, while the vector potential is advanced in time using either a simple explicit algorithm[32] or alternatively with a semi-implicit method which permits the time step to exceed the Courant limit.[33] Intuitively, this corresponds to an implicit treatment of light waves, while the rest of the algorithm remains explicit and the electron plasma frequency and cyclotron motion are fully resolved. For the present study, extensive comparisons between the two versions of the field solver have revealed no significant differences. The results presented in this manuscript were all obtained from the semi-implicit method which is nearly an order of magnitude faster for the parameter regime of interest.

The rectangular simulation domain shown in Fig. 1 has dimensions quite close to the actual experiment (150 cm $\times$75 cm), but does not exactly correspond to the detailed shape of the vessel wall. Physically, the time scale for diffusion of magnetic flux across the outer wall can be estimated by $\tau_R \approx \lambda_w^2/\mathcal{D}_M$, where λ_w is the thickness of the wall, $\mathcal{D}_M \equiv \eta c^2/(4\pi)$ is the magnetic diffusion coefficient, and η is the resistivity of the metal. Assuming a uniform cylinder with toroidal eddy currents, the L/R time for eddy current decay can be expressed as $\tau_{LR} \approx W\lambda_w/(2\mathcal{D}_M)$, where W is the radius of the cylinder. For a stainless steel wall with $\lambda_w \approx 6.4$ mm, the time scale for diffusion $\tau_R \approx 70$ μs is comparable to the characteristic time scale for the discharge $\sim$200 μs. The L/R time is $\tau_{LR} \approx 4.1$ ms for $W \approx 75$ cm, $W/(2\lambda_w) \approx 59$ times longer than τ_R. Since τ_{LR} is much longer than the discharge time scale, eddy currents may effectively prevent flux penetration; consistent with this calculation, very little magnetic flux has been measured outside of MRX. However, it is unlikely that the precise form of this boundary condition has a large influence on the structure of the electron layer; thus, for simplicity, at the outer wall, conducting boundary conditions are employed for the fields, while the particles are reflected elastically. As illustrated in Fig. 1, the simulation box contains two current carrying wires of radius $b=1.3$ cm within each flux core of radius $a=9.4$ cm. These dimensions, as well as the typical flux core spacing of $Z_0=40$ cm used in the cases presented in this paper, correspond to those of the experiment. The 2D Cartesian grid employed in these simulations covers the entire rectangular area shown in Fig. 1 including the inside of the flux cores. The surface of the flux core has a $\sim$0.1 mm layer of Inconel®-625 covering a dielectric core. Thus the time scale for flux diffusion $\tau_R \approx 0.01$ μs is much shorter than the discharge time scale and magnetic flux can freely penetrate. As a consequence, no field boundary condition is required at the surface of the flux cores. Instead, the flux cores are modeled entirely through the particle boundary condition. The region inside the flux cores is treated as a vacuum and particles that hit a flux core may be absorbed or reflected depending on a reflection coefficient parameter. Unless otherwise specified, simulations in this study absorb all particles that hit a flux core.

B. Dimensionless normalization of experiment

The simulations are performed in dimensionless units by scaling the geometry in Fig. 1 to the actual size of the experiment in terms of the ion inertial length $d_{i0}=c/\omega_{pi0}$, computed using a proton mass and the initial uniform density n_0. Thus, the number of ion inertial lengths between the flux cores in the simulation should closely match the actual experiment. The initial particle distributions are Maxwellian for both ions and electrons with temperature $T_{i0}=T_{e0}$. Working with dimensionless ratios, the initial plasma temperature is specified by v_{te0}/c, where $v_{te0} \equiv (2T_{e0}/m_e)^{1/2}$ is the electron thermal velocity. Another necessary dimensionless parameter is ω_{pe0}/Ω_{e0}, where $\Omega_{e0}=eB_0/(m_e c)$ is the electron cyclotron frequency evaluated using the reference magnetic field at a point 45° upstream from the flux cores (marked with an "X" in Fig. 1), while the electron plasma frequency ω_{pe0} is based on the initial uniform density n_0. Choosing these two dimensionless parameters effectively sets the plasma beta at this reference point,

$$\beta_{e0} \equiv \frac{8\pi n_0 T_{e0}}{B_0^2} = \left(\frac{\omega_{pe0}}{\Omega_{e0}}\frac{v_{te0}}{c}\right)^2.$$

Typical values for these dimensionless parameters in MRX are $v_{te0}/c \sim 0.003$, $\omega_{pe0}/\Omega_{e0} \sim 70$, and $\beta_{e0} \sim 0.04$. Note that v_{te0}/c corresponds to the ratio of the Debye length to the electron skin depth. Using realistic parameters, each skin depth would contain over 300 Debye lengths and kinetic simulations would be completely impractical since the cell size is typically set by the Debye length. In order to set up a simulation of manageable size, it is necessary to increase v_{te0}/c to reduce the large separation between the skin depth

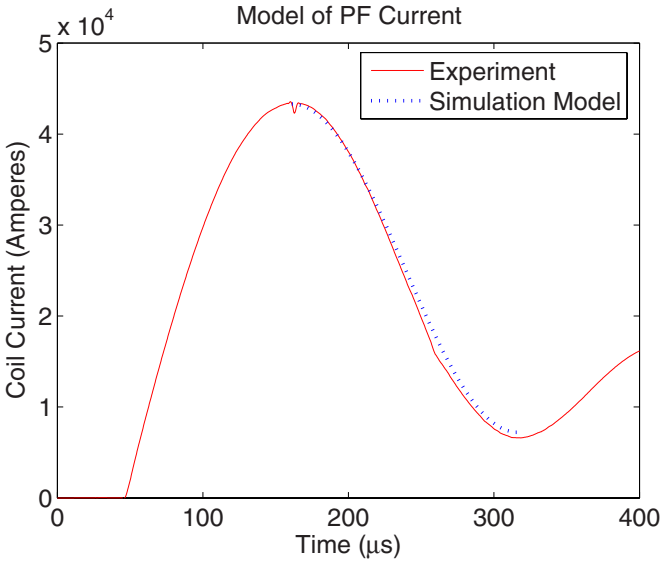

FIG. 2. (Color online) Comparison of the actual MRX poloidal field (PF) current waveform to the functional fit in Eq. (1) employed in this simulation study. For the case shown, the time scale of the current ramp-down $\tau = 155\ \mu s$.

and the Debye scales. At the same time, it is important to decrease the ratio of ω_{pe0}/Ω_{e0} in order to keep β_{e0} similar to realistic MRX values. Fortunately, a careful scan of initial temperature in the accessible parameter range $v_{te0}/c \approx 0.065-0.2$, while fixing $\beta_{e0}=0.059$ reveals no significant changes in the reconnection rate or electron layer scalings (see the Appendix for details).

The initial current in the flux cores, I_0, is selected to obtain the desired value of ω_{pe0}/Ω_{e0} at the reference point. The initial magnetic field is computed based on the current in the two wires and assuming a conducting boundary in which all the magnetic flux is contained within the vessel. The currents from the plasma are not included in this initial magnetic field, and the initial conditions do not correspond to an equilibrium. However, for the low β conditions under consideration, the plasma rapidly adjusts and the modifications to the vacuum field are rather small. As the simulation proceeds, the current in each flux core is reduced according to a sinusoidal waveform similar to the MRX coil current,

$$I = \frac{I_0}{6}\left[1 + 5\cos^2\left(\frac{\pi t}{2\tau}\right)\right]. \tag{1}$$

As shown in Fig. 2, this simple functional form is very close to the actual coil current in MRX. In this article, the parameter τ is referred to as the drive time of the simulation and controls how fast the current is ramped down.

Perhaps the most serious limitation of fully kinetic simulations is the large separation between ion and electron spatial and temporal scales. Using realistic MRX conditions for hydrogen plasmas, the domain size of 150 cm corresponds to $\sim 1500 d_{e0}$ or $\sim 30 d_{i0}$. Even with artificially high electron temperature $v_{te0}/c \sim 0.1$, this amount of scale separation is impractical for the present study, and thus it is necessary to employ an artificially heavy value for the electron mass in the range $m_i/m_e = 10 \rightarrow 150$. In order to overcome this limitation, the basic strategy is to match the experiment in terms of ion kinetic scales and then to examine the scaling of the results with the mass ratio m_i/m_e. These scalings allow us to extrapolate to realistic electron mass and search for parameters that do not depend on electron mass which can be compared to the experiment.

C. Energy conservation

Global energy conservation is an important consistency check to ensure the model is properly implemented. Maxwell's equations imply the following integral energy conservation equation for the fields

$$\frac{d}{dt}\int\left(\frac{B^2}{8\pi}+\frac{E^2}{8\pi}\right)dV + \int \mathbf{S}\cdot d\mathbf{a} + \int \mathbf{E}\cdot\mathbf{J}dV = 0, \tag{2}$$

where $\mathbf{S}=c(\mathbf{E}\times\mathbf{B})/4\pi$ is the Poynting flux. Since the outer wall is treated as perfect conductor, there is no flow of electromagnetic energy across this surface and the second term is identically zero for this problem. The current density in the last term includes both the plasma currents $\mathbf{J}_p$ and the prescribed currents in the flux cores $\mathbf{J}_c$. The energy conservation equation for the particles is

$$\frac{d}{dt}\left(\sum_j \frac{m_j v_j^2}{2} + W_{\text{lost}}\right) - \int \mathbf{E}\cdot\mathbf{J}_p dV = 0, \tag{3}$$

where the summation is over particles in the plasma and W_{lost} is the kinetic energy of particles absorbed at the flux cores. Adding Eqs. (2) and (3) results in the total energy conservation equation for the system. Notice that the $\mathbf{E}\cdot\mathbf{J}_p$ terms cancel, while the $\mathbf{E}\cdot\mathbf{J}_c$ represents the loss of electromagnetic energy through the flux cores. For the simulations presented in this manuscript, deviations from this total energy conservation equation are typically less than 1%, which is comparable to a closed periodic system with standard boundary conditions.

III. CURRENT LAYER STRUCTURE

A. Formation and structure

In order to illustrate the basic features and time evolution of the simulations in this study, first consider a case with initial plasma density $n_0 = 2\times 10^{13}\ \text{cm}^{-3}$, corresponding to a flux core spacing of $Z_0 \approx 7.8 d_{i0}$. The spatial grid for this example is 2560×1280 with 2×10^9 particles and a time step $\Delta t \Omega_{e0} = 0.12$. The mass ratio is $m_i/m_e = 150$ and the drive time is $\tau\Omega_{i0} = 150$. As discussed in the previous section, the initial configuration corresponds to a uniform plasma with no reconnection. However, as the coil current is reduced according to Eq. (1), the flux surfaces are pulled towards the cores and a current layer is gradually formed, as illustrated in Fig. 3. In this time sequence, the top panel shows the entire simulation domain, while the subsequent panels show the region of interest between the flux cores where the reconnection layer develops. As the simulation proceeds, the thickness of the electron layer in Fig. 3 remains approximately constant, while the length gradually expands.

During the time range $0.5 \lesssim t/\tau \lesssim 0.7$, the reconnection process is approximately steady and the overall structure re-

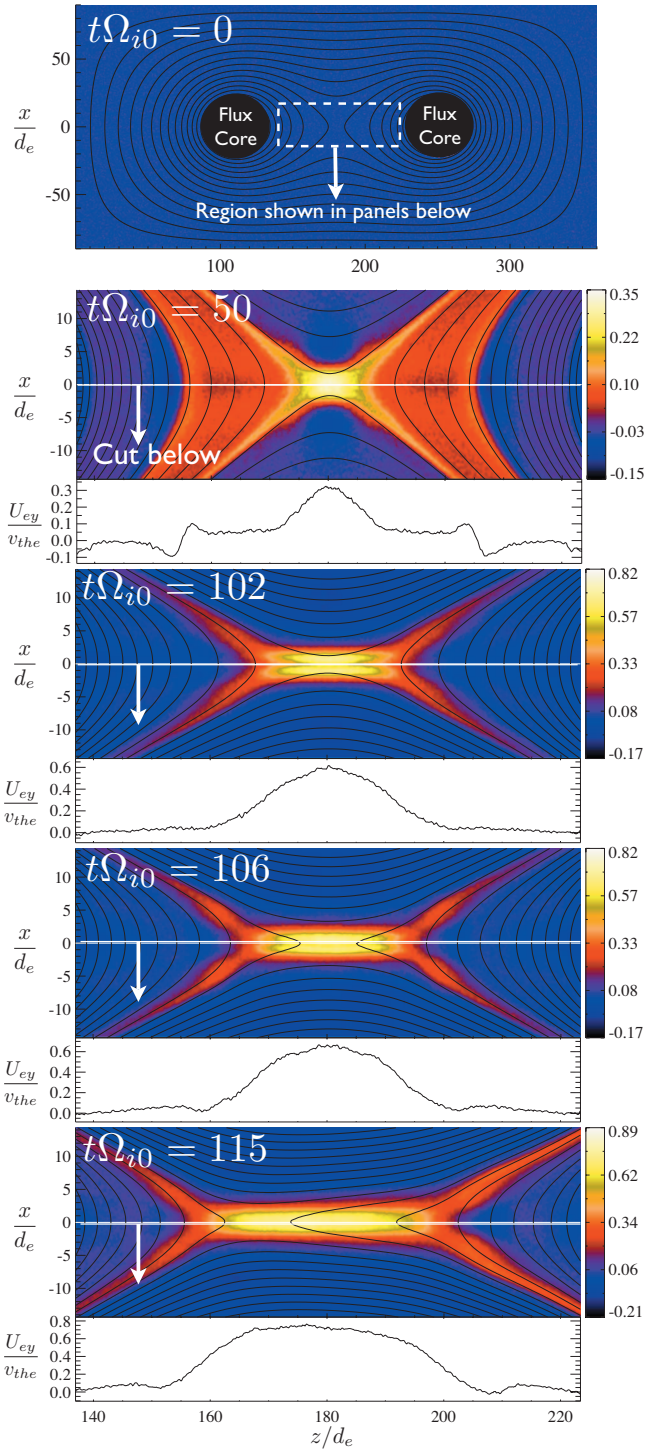

FIG. 3. (Color) Time evolution of the electron current sheet for a simulation with dimensionless parameters $m_i/m_e=150$, $\tau\Omega_{i0}=150$ (equivalent to $\tau/\tau_{A0}=19.1$), $\beta_{e0}=0.067$, $v_{te0}/c=0.16$, and full particle absorption at the flux core surfaces. The initial density is $n_0=2\times10^{13}$ cm^{-3} corresponding to a flux core spacing of $Z_0=7.8d_{i0}$. Shown is out-of-plane component of the electron flow $U_{ey}\approx-J_y/(ne)$ normalized to the initial electron thermal velocity v_{te0}; black lines correspond to the magnetic flux surfaces. Movie showing the evolution is available in Ref. 38.

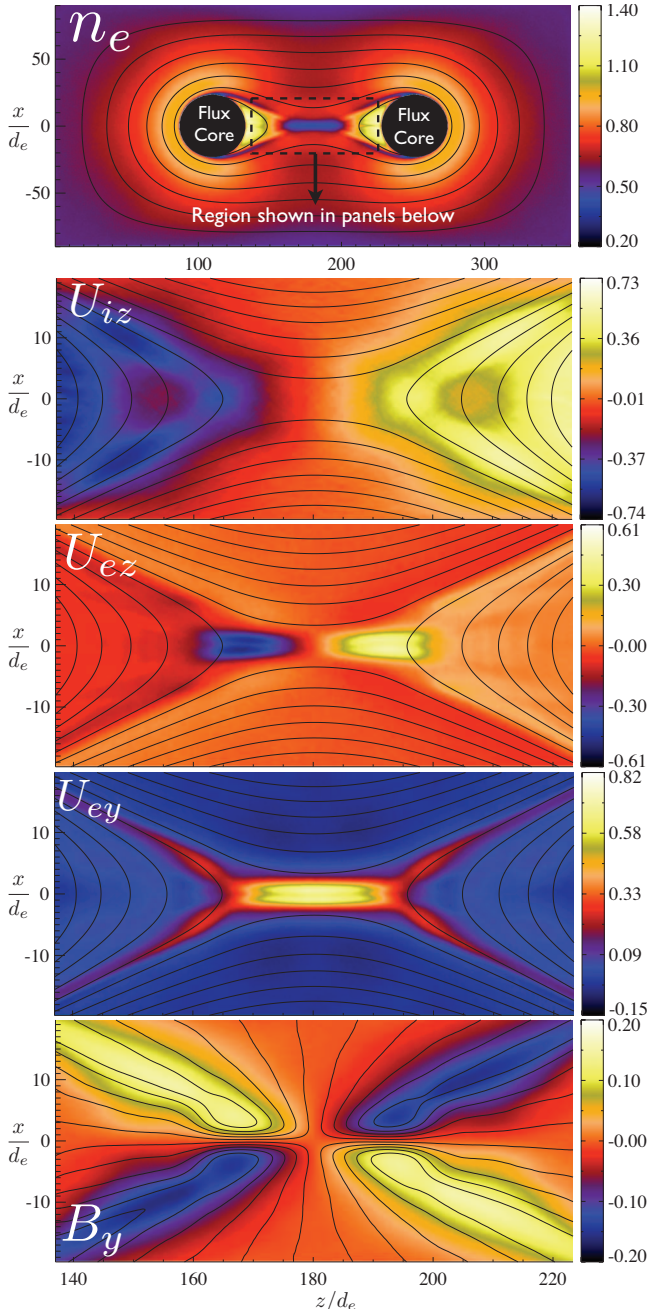

FIG. 4. (Color) Typical structure of the reconnection layer for the same case as Fig. 3 at time $t\Omega_{i0}=105$. Top panel shows the electron density for the entire global domain while subsequent panels show various quantities of interest within the window indicated in the top panel. Black lines represent flux surfaces in all panels except the bottom, where the black lines indicate the streamlines for the electron flow. The density is normalized to n_0, the ion and electron flow velocities are normalized to the initial thermal velocity for each species and B_y is normalized to the initial reference magnetic field B_0.

sembles that observed in many other kinetic simulations. The essential features are illustrated Fig. 4 at the simulation time $t\Omega_{i0}=105$. To illustrate the global simulation geometry, the top panel shows the plasma density for the entire simulation domain while the subsequent panels illustrate the basic structure of the reconnection layer in the region indicated between the flux cores. As expected, there are strong density gradients as plasma builds up around the flux cores, while the density is depleted in the center of the layer. It should be noted that no density hole is observed in the experiment; however, this may be due to insufficient Langmuir probe resolution. Since ions and electrons become demagnetized on different spatial scales, the ion outflow channel is significantly broader com-

pared to the narrow electron layer, as illustrated in the next two panels. In particular, the half width of the ion outflow channel is on the order $\sim 1.5 d_{i0}$, while the electron channel is approximately $\sim 2 d_{e0}$. At this particular time, the half length of the out-of-plane current sheet is $\sim 12 d_{e0}$. The separation between the electron and ion scales gives rise to the familiar quadrupole magnetic field pattern shown in the bottom panel along with the streamlines for the in-plane electron flow. Although this particular example is consistent with many previous kinetic studies, it is important to note that the structure of the layer in the outflow direction is strongly influenced by both the drive time and the downstream boundary condition. In simulations with relatively strong drive (i.e., relatively short drive time), the electron current layer is unstable to plasmoid formation at the later stages of the evolution in a manner similar to recent open boundary kinetic simulations.[2] In the following section, the important issue of drive time is examined in a systematic fashion.

B. Drive time and reconnection rate

In order to analyze the dependence of the reconnection process on the external forcing, the drive strength was varied in this study over a fairly wide range by varying the characteristic time scale τ for the current ramp-down in Eq. (1). One useful diagnostic to characterize the evolution is the normalized reconnection electric field at the center of the simulation box

$$E_R = \frac{cE_y}{B_0 v_{A0}}, \tag{4}$$

where B_0 is the reference value of the magnetic field and $v_{A0}=B_0/(4\pi n_0 m_i)^{1/2}$ is the corresponding value of the Alfvén speed computed with the initial density. In order to eliminate high frequency noise, the electric field E_y is time-averaged over a window $\pm\Omega_{io}^{-1}$. The upper panel of Fig. 5 shows E_R as function of simulation time for a range of different simulations at $m_i/m_e=75$ and $n_0=2\times 10^{13}$ cm^{-3}, in which the drive τ time is varied relative to the Alfvén time $\tau_{A0}=Z_0/v_{A0}$ based on the flux core spacing Z_0. During the first half of the simulation, the current layer forms and the electric field increases. In the latter half of the simulation, the field plateaus and decreases slightly. During the time interval $0.5 \lesssim t/\tau \lesssim 0.7$, the basic structure of the electron layer is changing slowly (i.e., quasi-steady) and thus it is interesting to examine how the average field $\langle E_R \rangle$ over this interval scales with the drive time. This scaling is shown in the bottom panel of Fig. 5 as function of τ_{A0}/τ. Simulations with a range of initial densities $n_0=(1.25-8)\times 10^{13}$ cm^{-3} and mass ratios $m_i/m_e=10-150$ are used in the scaling, but all cases have constant box geometry and $\beta_{e0}\sim 0.06$. For relatively weak forcing, i.e., relatively large values of τ, the average electric field at the center scales linearly with $1/\tau$. Thus, as illustrated in Fig. 5, the scaling of a normalized electric field can be conveniently expressed as

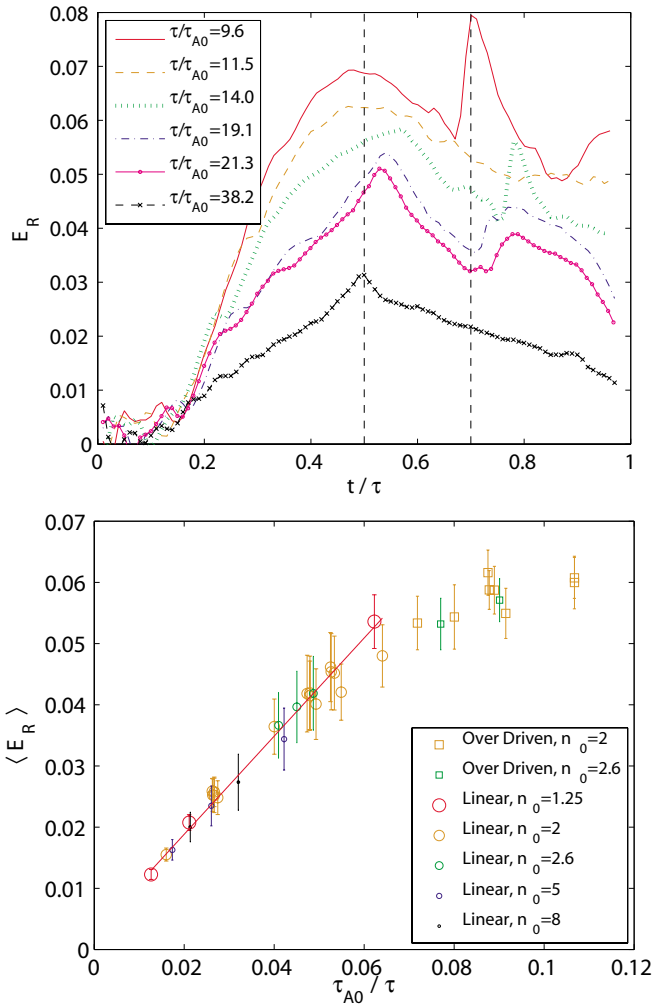

FIG. 5. (Color online) Normalized electric field at the center of the layer $E_R=cE_y/(B_0 v_{A0})$ as a function of simulation time for various drive time times τ/τ_{A0} indicated (top). The parameters are $m_i/m_e=75$, and $n_0=2\times 10^{13}$ cm^{-3}. The bottom panel shows the scaling of the average electric field $\langle E_R \rangle$ in the quasi-steady interval $(0.5-0.7)\tau$ (indicated by vertical dashed lines in upper panel); error bars represent the standard deviation due to the time average. Simulations include a range of initial densities $n_0=(1.25-8)\times 10^{13}$ cm^{-3} and mass ratios $m_i/m_e=10-150$, but all cases have constant box geometry and $\beta_{e0}\sim 0.06$. Some cases in the over-driven regime have a reflection coefficient parameter of 0.1 or 0.2 to prevent magnetic island formation (see Sec. III E). Circle sizes represent different initial densities; values given for n_0 assume hydrogen ions and are in units of 10^{13} cm^{-3}.

$$\langle E_R \rangle = \frac{c\langle E_y \rangle}{B_0 v_{A0}} \propto \frac{\tau_{A0}}{\tau}, \tag{5}$$

where $\langle\ \rangle$ represents a time average over the quasi-steady interval $(0.5 \lesssim t/\tau \lesssim 0.7)$. In the limit of short drive time $\tau \lesssim 16\tau_{A0}$, the dependence of the average electric field on τ levels off and saturates. These results allow us to divide the simulations into two different regimes based on the strength of the drive:

(1) **Linear regime**. The plasma responds on the same time scale as the drive. The reconnection electric field $\langle E_R \rangle$ scales linearly with $1/\tau$, as shown in the lower panel of Fig. 5. The electron layer length displays a strong dependence on the drive time, while the layer width shows

only a weak dependence, as discussed in Sec. III D.

(2) **Over-driven regime**. The plasma cannot respond on the same time scale as the drive. Depending on the flux core boundary conditions (see Sec. III E), secondary magnetic islands (or plasmoids) may form that break up the layer.

The mechanism responsible for saturation of the electric field in the over driven regime is still an open question. Note that no flux pile-up is observed in the present study for either the linear or over driven regimes. At the present time, it appears that MRX operates within the linear regime but no detailed experimental study has yet been performed. In the simulations, there is some uncertainty in precisely how to set the drive time due to the use of artificially heavy electron mass. The range of values chosen in this study correspond fairly well with rough estimates based on the number of global Alfvén times and/or Ω_{i0} time scales. A more precise method to choose the appropriate drive time is described in the following section.

C. Inflow and outflow regions

By appropriately choosing the drive time, it is possible to closely match some of the experimentally measured features of the layer, such as the inflow of magnetic flux into the reconnection region. In order to compare the inflow between simulation and experiment, it is important to normalize the local inflow velocity by the local Alfvén velocity,

$$E_R(X) = \frac{cE_y}{B(X)v_A(X)}, \tag{6}$$

where the electric field E_y is time-averaged over a window $\pm\Omega_{io}^{-1}$ to eliminate high frequency noise, $B(X)$ is the magnetic field at a distance X upstream from the center of the current layer, and $v_A(X)$ is the Alfvén speed computed using $B(X)$ and the plasma density line-averaged along the length of a flux core diameter in the inflow region. Consistent with most reconnection literature, the reconnection rate $E_R^* \equiv E_R(X=d_i)$ is defined based on this normalized inflow velocity evaluated at one ion inertial length upstream. In contrast to Eq. (4), this normalization captures systematic variations in the upstream conditions and thus produces a meaningful dimensionless number for the reconnection rate that is useful for comparisons with MRX.

The time evolution of the normalized reconnection rate E_R^* is shown in the top panel of Fig. 6 for the various drive times indicated. These simulations correspond to the same set of cases used in the top panel of Fig. 5. Note that during the period $0.5 \lesssim t/\tau \lesssim 0.7$ the reconnection rate is quasi-steady and it is interesting to examine the scaling of the average rate $\langle E_R^* \rangle$ during this interval with drive time. This is shown in bottom panel of Fig. 6 for the same set of cases as considered previously in bottom panel of Fig. 5. Note that the properly normalized reconnection rate $\langle E_R^* \rangle$ also displays a linear scaling with $1/\tau$ for weak drive followed by a saturation for strong drive. In contrast to the clean break in Fig. 5, the transition in Fig. 6 is more gradual. This results in a

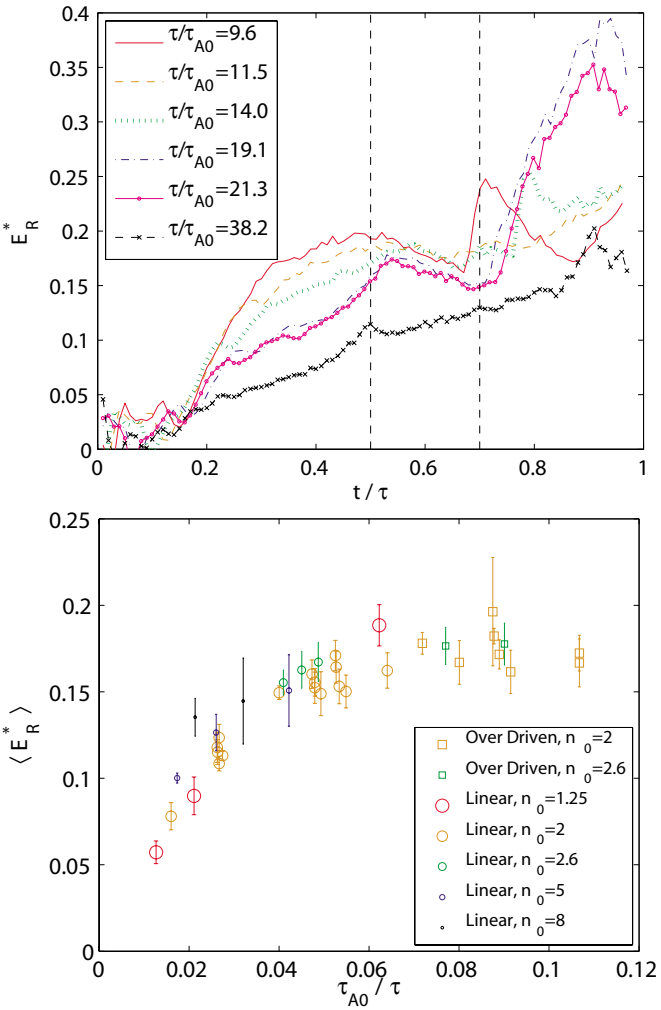

FIG. 6. (Color online) Reconnection inflow rate E_R^* as a function of simulation time for the various drive times τ/τ_{A0} indicated (top). The bottom panel shows the time-averaged rate $\langle E_R^* \rangle$ over the quasi-steady interval $(0.5-0.7)\tau$ as function of drive time τ_{A0}/τ. Parameters and notation are the same as Fig. 5.

weaker dependence on the drive time in the upper portion of the linear regime; in this region an increase in upstream B compensates for the increase in E_y.

Part of the strategy to properly match the drive time between simulation and experiment is to compare the spatial profile of the normalized MHD inflow velocity $E_R^*(X)$ [Eq. (6)] computed from the relevant electric and magnetic fields. A typical example is illustrated in Fig. 7 for a case with $m_i/m_e=75$, $n_0=2.6\times10^{13}$ cm^{-3}, and $\tau\Omega_{i0}=185$ $(\tau/\tau_{A0}=20.7)$. For this particular choice of drive, the dimensionless inflow velocity is in excellent agreement with experiment for $x>0$, implying a close match in the reconnection rate. As evident in Fig. 7 for $x<0$, the toroidal geometry of MRX introduces additional complications into this match, since the field generated by the toroidally symmetric coils is larger towards the inside of the device, resulting in a faster Alfvén speed and hence a lower normalized inflow than in the region closer to the outer wall. Thus, it is not possible to simultaneously match the inflow on both sides. However, this matching procedure guarantees that the overall strength of the drive is quite similar between simulation and experiment.

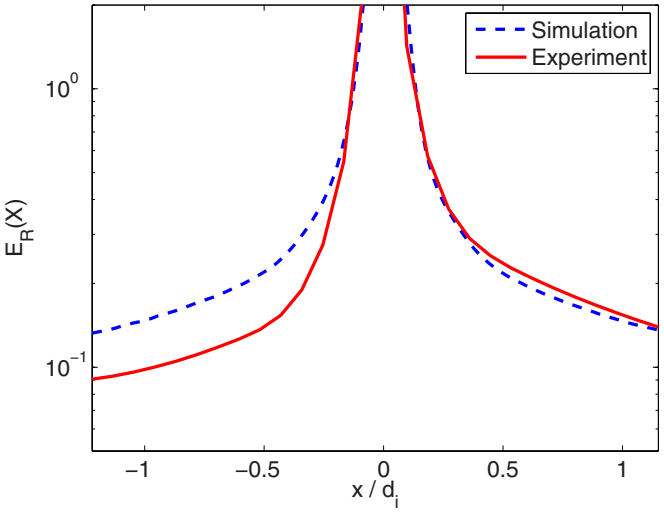

FIG. 7. (Color online) Normalized inflow speed $E_R(X)$ profile [as defined by Eq. (6)] at $t=0.7\tau$ for a well-matched simulation compared with MRX measurements for a hydrogen discharge. Simulation parameters are $\tau\Omega_{i0}=185$ ($\tau/\tau_{A0}=20.7$), $n_0=2.6\times10^{13}$ cm^{-3}, $m_i/m_e=75$, $\beta_{e0}=0.059$, and no reflection at the flux core surfaces. There is a mismatch on the inboard side of MRX due to toroidal geometry effects not included in the simulation.

The outflow region for this particular example is also well-matched, as illustrated in Fig. 8 comparing the quadrupole magnetic field and flow profiles. For this particular case, both the ion-scale and electron-scale features are in good agreement between the simulation and experiment. However, this is misleading for the electron-scale features due to the artificial mass ratio $m_i/m_e=75$ employed in this simulation. In the next section, we systematically examine the scaling of the electron layer with this parameter in order to better understand the scaling to the physically relevant parameters. The important point in Fig. 8 is that it is possible to closely match the ion-scale features between experiment and simulation despite the difference in m_i/m_e. In general, the structure of the out-of-plane quadrupole magnetic field varies with the drive time. If the simulation is over-driven, the electron channel opens abruptly in the outflow region, a feature that is not consistent with the structure seen in the experiment. By contrast, most simulations in the linear regime display no such opening. However, if the drive is too weak, then the peak B_y/B_z ratio will be too small compared to the experiment. Thus, an intermediate drive time $\tau\Omega_{i0}=185$ results in the best agreement for these features, as illustrated in Fig. 8.

D. Scaling of electron layer

As demonstrated in the previous section, it is possible to closely match the ion-scale features in MRX by appropriately choosing the drive time in the 2D kinetic simulations. However, this does not necessarily mean that the simulations have correctly captured all of the physics. For the linear regime, it is clear from Fig. 5 that the reconnection rate $\langle E_R\rangle$ is set predominantly by the drive time; thus, the reconnection layer must adjust to accommodate the drive. In order to fully understand the physics, it is essential to consider how the

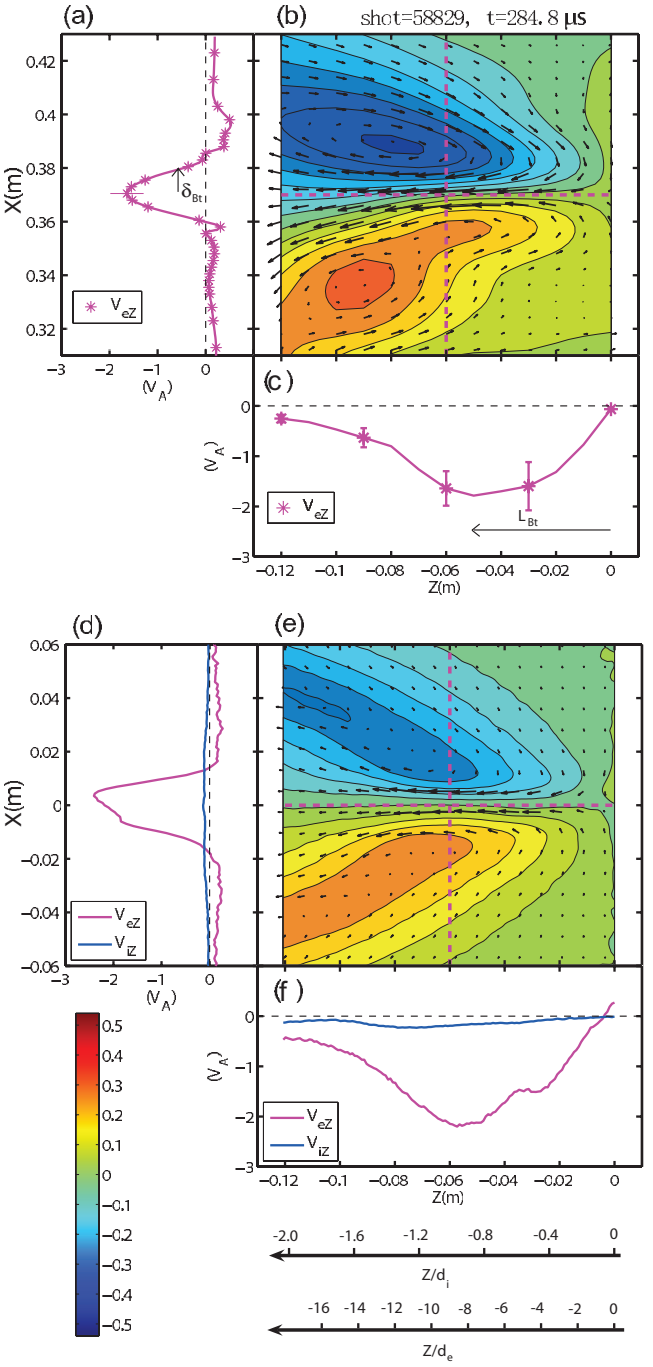

FIG. 8. (Color) Structure of the electron layer from experimental data [panels (a)–(c)] compared with the well-matched simulation from Fig. 7 [panels (d)–(f)]. Arrows in panels (b) and (e) represent in-plane electron flow; the color scale in the two figures is identical and represents B_y/B_z, where B_z is measured at $2\delta_{Bz}$ (δ_{Bz} is a half-layer width based on a Harris sheet fit to the B_z profile) and B_y is measured at the point in question. Note that although the electron layer dimensions in centimeters are the similar in the simulation and experiment, due to the artificial mass ratio $m_i/m_e=75$ used in the simulation, the dimensions in terms of electron skin depths do not match.

detailed structure of the electron layer scales with m_i/m_e in the simulation and compare these trends with experiment.

To facilitate this comparison, consistent definitions are required. The layer length L_{Bt} is defined as the distance from the X-point to the location of peak electron outflow. The layer thickness δ_{Bt} is defined by the half width of the V_{ez}

profile at 40% of the maximum at the location of peak electron outflow. These definitions are illustrated in panels (a) and (c) of Fig. 8. L_{Bt} and δ_{Bt} define the electron dissipation region; this was checked in several simulations to correspond well to a region where $\boldsymbol{E}\cdot\boldsymbol{J}$ is nonzero.

Since there is always some uncertainty in choosing the drive time, we consider the influence of both m_i/m_e and τ on the structure of the electron layer. A mass ratio scan was performed in the range $m_i/m_e=10\rightarrow 150$ for three different drive times: $\tau\Omega_{i0}=90$, 150, 300 ($\tau/\tau_{A0}=11.5$, 19.1, 38.2). For all runs, the ion scaling was fixed such that $d_i\approx 5$ cm during the quasi-steady-state portion of the run. As illustrated in the top panel of Fig. 9, the thickness of the electron layer is observed to scale approximately linearly with the electron skin depth d_e computed using the line-averaged density at the relevant simulation times, with similar weak power law dependencies on both m_i/m_e and $\tau\Omega_{i0}$. The power law exponents on the fitted curves shown are 0.13 ± 0.01, 0.15 ± 0.02, and 0.17 ± 0.02 for drive times of $\tau\Omega_{i0}=90$, 150, and 300, respectively. When scaled by $\tau\Omega_{i0}$ raised to the one-sixth power, the three curves approximately overlap.

The bottom panel of Fig. 9 also shows an extrapolation to realistic mass ratio using this weak dependence. Square symbols represent the layer thickness in the experiment which is approximately $8d_e$ for all three gases used. Extrapolating the 0.18 ± 0.01 power law scaling at the drive time of $\tau\Omega_{i0}=185$ (which was found to be well-matched to a hydrogen discharge in Figs. 7 and 8), the result is only $\delta_{Bt}\approx 3d_e$ at realistic hydrogen mass ratio, an estimate that is significantly below the lower error bar of the experimental measurement. Extrapolation to deuterium and helium mass ratios is less certain because the drive has not been matched, but the extrapolation leads to an estimate that is still well below the experimental value for a range of likely drive times. Thus, the mass ratio limitation is unlikely to be responsible for the broader electron layers in the experiment.

For cases well within the linear regime where a clear scaling is possible, the layer length L_{Bt} displays a mass ratio scaling similar to the thickness during the quasi-steady-state time period. This is illustrated in the top panel of Fig. 10, where the aspect ratio is plotted as a function of time for four different mass ratios at a long drive time of $\tau\Omega_{i0}=300$. During the quasi-steady-state period the four curves approximately overlap, indicating that the aspect ratio of the layer is electron mass independent for this set of parameters. Therefore, extrapolation to realistic mass ratio should not affect the aspect ratio of the layer. This means that because the width that results from this extrapolation is too small compared to the experiment, the length that results from the same extrapolation will also be too small by a similar factor.

However, despite this estimate, a clear scaling for the length of the layer is difficult to obtain. As can be seen from the time evolution of the aspect ratio and from Fig. 3, the layer is lengthening during the quasi-steady-state period, so any scaling is dependent on the time period chosen. Furthermore, as seen in the bottom panel of the figure where the aspect ratio is plotted for a variety of drive times, the point in time at which the layer lengthens as well as the lengthening rate is highly sensitive to the drive. All six cases start with an aspect ratio $\sim 1.5-2$ at $t=0.25\tau$, but as the simulation evolves, the subsequent evolution varies widely. In the overdriven case, i.e., $\tau/\tau_{A0}=9.6$, a magnetic island forms near 0.7τ, which leads to a collapse in the length of the layer. Neither layer lengthening nor magnetic islands have been conclusively identified in the experiment, further complicating comparisons.

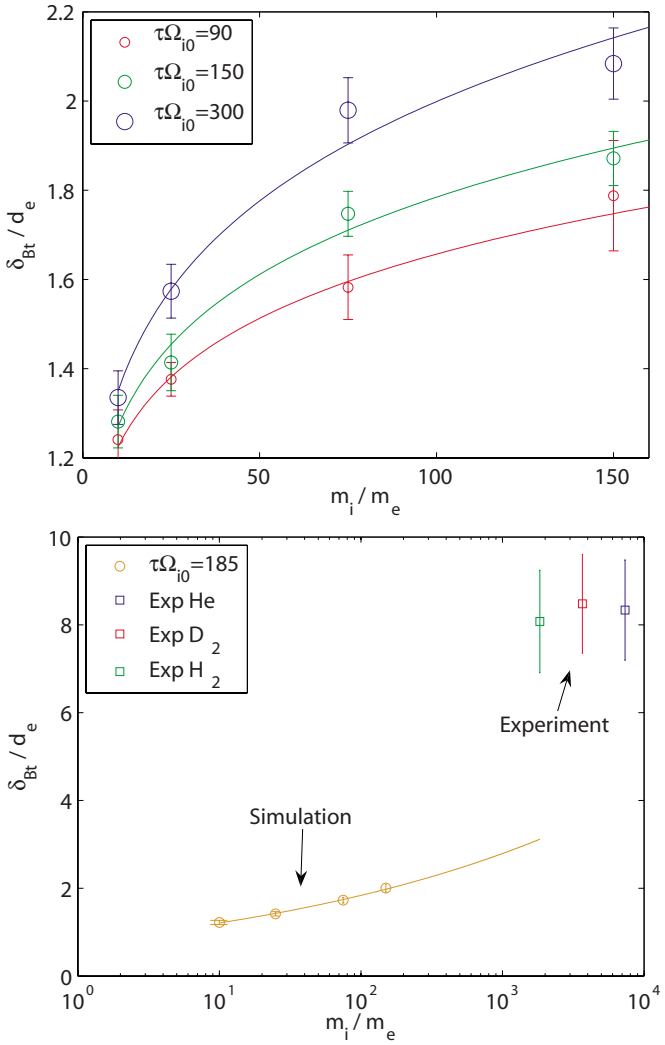

FIG. 9. (Color online) Scaling of the electron layer thickness in simulation compared with experiment. Electron layer thickness in units of d_e, an election skin depth computed using the line-averaged density between the flux cores at the time of comparison, as a function of m_i/m_e is plotted for three different drive times (top). All other quantities are held fixed in terms of ion units; relevant parameters are $n_0=2\times 10^{13}$ cm^{-3} and $\beta_{e0}\sim 0.06$. Data are averaged over the quasi-steady interval $t=(0.5-0.7)\tau$, error bars in the simulation data represent the standard deviation from this averaging. In all three cases, the layer thickness scales approximately as $\delta_{Bt}/d_e\propto(m_i/m_e)^{1/6}$; exponents for each curve are given in the text. In the bottom panel, the same scaling is shown using $n_0=2.6\times 10^{13}$ cm^{-3} and $\tau\Omega_{i0}=185$, parameters from the case that best matches a hydrogen discharge. Experimental data are shown with error bars from a fit of the layer width as a function of d_e; an extrapolation curve to realistic hydrogen mass ratio is shown. This extrapolation yields a layer width of $\delta_{Bt}\sim 3d_e$.

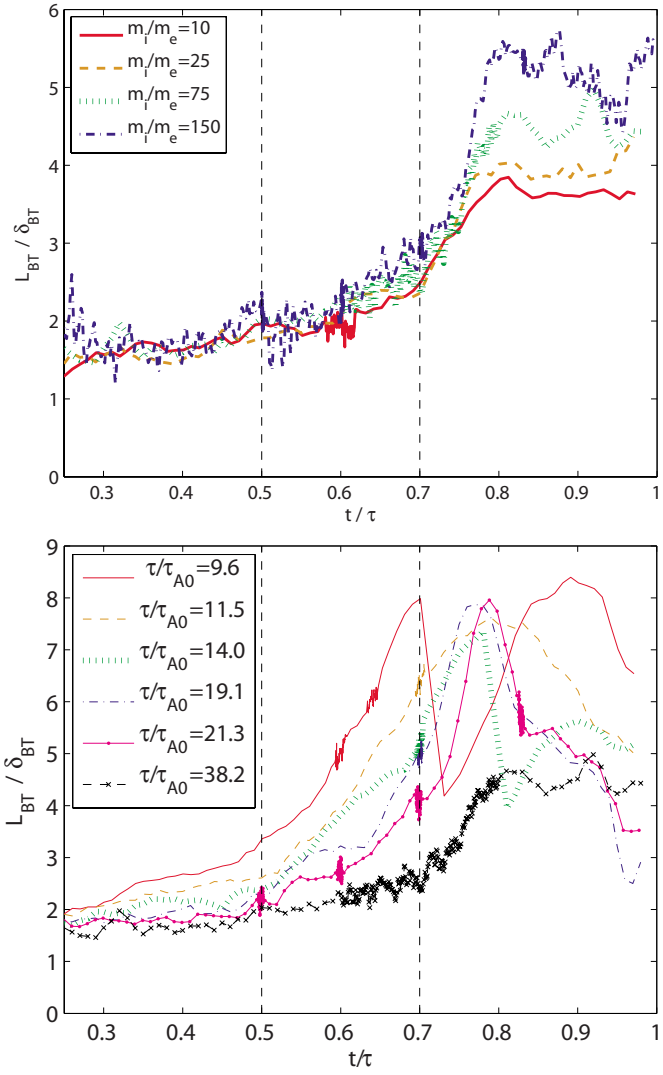

FIG. 10. (Color online) Aspect ratio of the electron layer as a function of time for various m_i/m_e (top) and drive times (bottom). Relevant parameters are $n_0=2\times10^{13}$ cm^{-3} and $\beta_{e0}\sim0.06$. In the top panel, $\tau\Omega_{i0}=300$ ($\tau/\tau_{A0}=38.2$); in the bottom panel, $m_i/m_e=75$. The boundary of the quasi-steady interval ($0.5-0.7\tau$) is marked on both panels by vertical dashed lines. Particles are absorbed at the flux core boundaries for all cases except for $\tau/\tau_{A0}=9.6$, which has a reflection coefficient of 0.1 and $\tau/\tau_{A0}=11.5$, which has a reflection coefficient of 0.2.

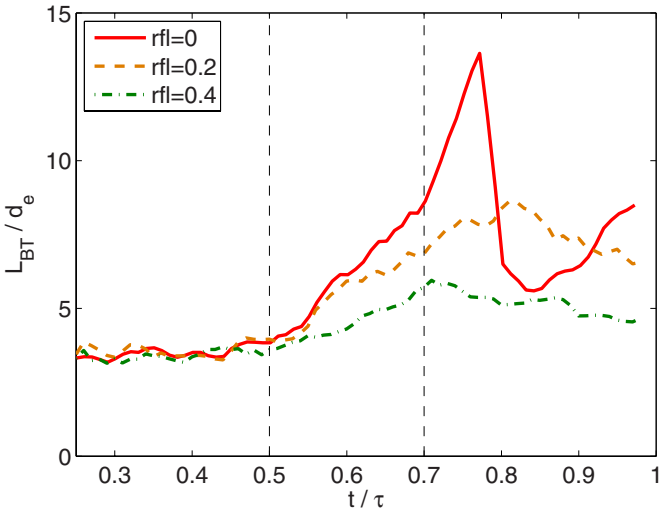

FIG. 11. (Color online) Layer length as a function of time for three different reflection coefficients. Reflection inhibits elongation of the layer in the quasi-steady-state region and prevents island formation. Simulation parameters are $m_i/m_e=25$, $n_0=2\times10^{13}$ cm^{-3}, $\tau\Omega_{i0}=100$ ($\tau/\tau_{A0}=12.7$), and $\beta_{e0}=0.059$.

E. Flux core particle boundary conditions

Most simulations presented thus far employed a particle boundary condition at the flux core corresponding to complete absorption of particles. This boundary condition has a large influence on the downstream pressure and thus can have a significant influence on the structure of the reconnection layer. To demonstrate the sensitivity to this boundary condition, Fig. 11 illustrates the length of the electron layer as a function of time for three simulations in which the reflection coefficient was varied from $0\%\rightarrow40\%$. Randomly reflecting some fraction of the particles results in higher downstream pressure, which limits the length of the electron layer while leaving the thickness unchanged. The sensitivity to this boundary condition makes comparisons with experimental measurements of the layer length difficult, since the precise nature of the particle boundary condition at the flux core is unknown.

In the over-driven regime with full particle absorption at the flux cores, large islands develop near the layer center and are ejected into the outflow region, shortening the layer and inhibiting clear scaling results. When a small fraction (typically ~0.2) of particles are reflected at the flux core surfaces, the resulting downstream pressure buildup inhibits layer lengthening, and island formation may be suppressed. However, despite this change in the aspect ratio due to reflection, the reconnection rate as measured by the electric field at the center of the layer typically remains unchanged, except at times where large magnetic islands dominate the simulation. This is simply another indication that the average reconnection rate in these driven simulations is predominantly set by the drive time.

IV. DISCUSSION

A. Scaling for reconnection electric field

In the absence of a guide field, the thickness of the electron layer in PIC simulations corresponds approximately to the scale of the meandering electron orbits in the central region of the current sheet

$$\delta_M \sim \sqrt{\frac{\delta_{Bt} v_{te}}{\Omega_e}}, \tag{7}$$

where δ_{Bt} is the characteristic scale length of the magnetic field reversal and Ω_e is the upstream cyclotron frequency at the layer edge. This observation allows one to obtain an approximate model of the electron diffusion region. Indeed, consider a sketch of the electron layer shown in Fig. 12. Electrons enter the layer with an inflow speed $v_{\rm in}$, equal to the local $\boldsymbol{E}\times\boldsymbol{B}$ velocity, and leave it with an outflow speed $v_{\rm out}$. Assuming incompressibility,

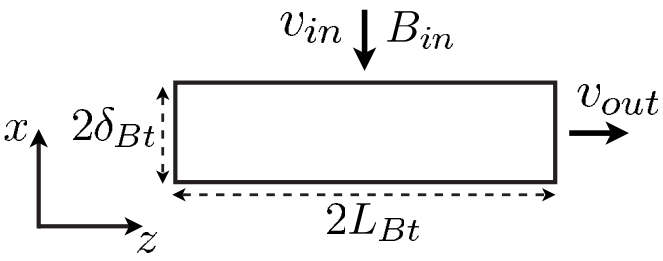

FIG. 12. Sketch of the electron layer.

$$v_{\text{in}} = \frac{cE_y}{B_{\text{in}}} \sim \frac{\delta_{Bt}}{L_{Bt}} v_{\text{out}}. \tag{8}$$

Since the meandering electron population can respond freely to the reconnection electric field, physically one would expect the characteristic scale of this current layer to be roughly $\delta_{Bt} \sim \delta_M$, which implies

$$\delta_{Bt} \sim \delta_M \sim \frac{v_{te}}{\Omega_e}, \tag{9a}$$

$$\frac{B_{\text{in}}\delta_{Bt}}{c} \sim \frac{\sqrt{2m_eT_e}}{e}. \tag{9b}$$

Combining Eqs. (9b) and (8) yields an expression for the reconnecting electric field:

$$E_y \sim \frac{\sqrt{2m_eT_e}}{e}\frac{v_{\text{out}}}{L_{Bt}} \sim \frac{\sqrt{2m_eT_e}}{e}\frac{\partial v_{ez}}{\partial z} \equiv E_{\text{NG}}. \tag{10}$$

This is the same expression that was derived in Ref. 7 starting from a model for the nongyrotropic electron pressure tensor and also assuming that the layer thickness is set by the meandering orbit scale.

Expression (9a) is a good estimate for the thickness of the electron layer in the 2D kinetic simulations, but fails to reproduce the experimental data from MRX. This is demonstrated in Fig. 13, where the electron layer thickness is plotted against the meandering orbit scale δ_M, as defined by Eq. (9a), in both the simulation and experiment. While the layer thickness observed in the simulations scales linearly with δ_M, the spread of the experimental data points indicates that there is no clear relationship between δ_M and the experimentally measured layer thickness. Also note that the values reported for the simulations correspond to artificially large electron mass. Extrapolation to realistic hydrogen mass ratio based on the result presented in Sec. III D yields the values $\delta_{Bt} \sim 3d_e$.

B. Electron layer force balance

The discrepancy in the electron layer thickness that was discussed in the previous section may have important implications for the electron layer force balance. Indeed, all the assumptions made in Sec. IV A hold in the simulations and the out-of-plane electric field is well approximated by the expression for E_{NG} in Eq. (10), as shown in the top panel of Fig. 14. However, E_{NG} is too small to account for the experimentally observed reconnection electric field. This is illustrated in the bottom panel of Fig. 14, where Eq. (10) is compared to the experimental measurements.

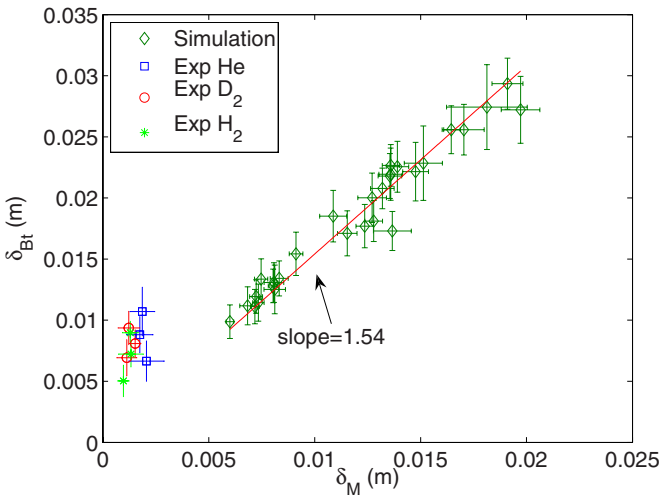

FIG. 13. (Color online) Layer width as a function of the meandering orbit width $\delta_M = v_{te}/\Omega_e$; simulation data are averaged over $t = (0.5-0.7)\tau$; error bars represent the standard deviation due to this averaging. Linear regime cases from Fig. 5 are shown. The layer width agrees with the meandering orbit calculation up to a factor of 1.6 in the simulation, but does not match δ_M in the experiment.

Expression (10) may be interpreted as the contribution to the experimentally observed reconnection electric field due to the nongyrotropic components of the electron pressure tensor (hence the subscript NG). This explanation would lead to the conclusion that the physical mechanism responsible for balancing electric field in the experiment differs significantly from that in the simulations. However, a word of caution is in order. The derivation of E_{NG} presented in the previous section depends crucially on the assumption that the thickness of the current layer is approximately set by the meandering orbit scale δ_M. Similarly, other ways of obtaining that estimate (e.g., Refs. 7 and 34) make certain assumptions concerning the structure of the electron layer that may be violated in the experiments. Thus, we are lead to conclude that at the present time the question of what is the physical mechanism responsible for supporting the reconnection electric field in the experiment remains open. Further studies that include the effects omitted from the simulations presented here, namely, 3D geometry and binary collisions, are needed in order to provide an unequivocal answer.

Another possibility to obtain further information on the nature of the electric field would be to systematically compare the drive time scalings of the electric field between the simulations and the experiments. In particular, the value of the drive time where the scaling deviates from the linear one and the corresponding value of the electric field may provide additional information concerning the physics of the reconnection layer. However, because of differences in the plasma production process between the simulation and experiment which affect the early evolution prior to the quasi-steady-state period, such a comparison is nontrivial and has not yet been performed.

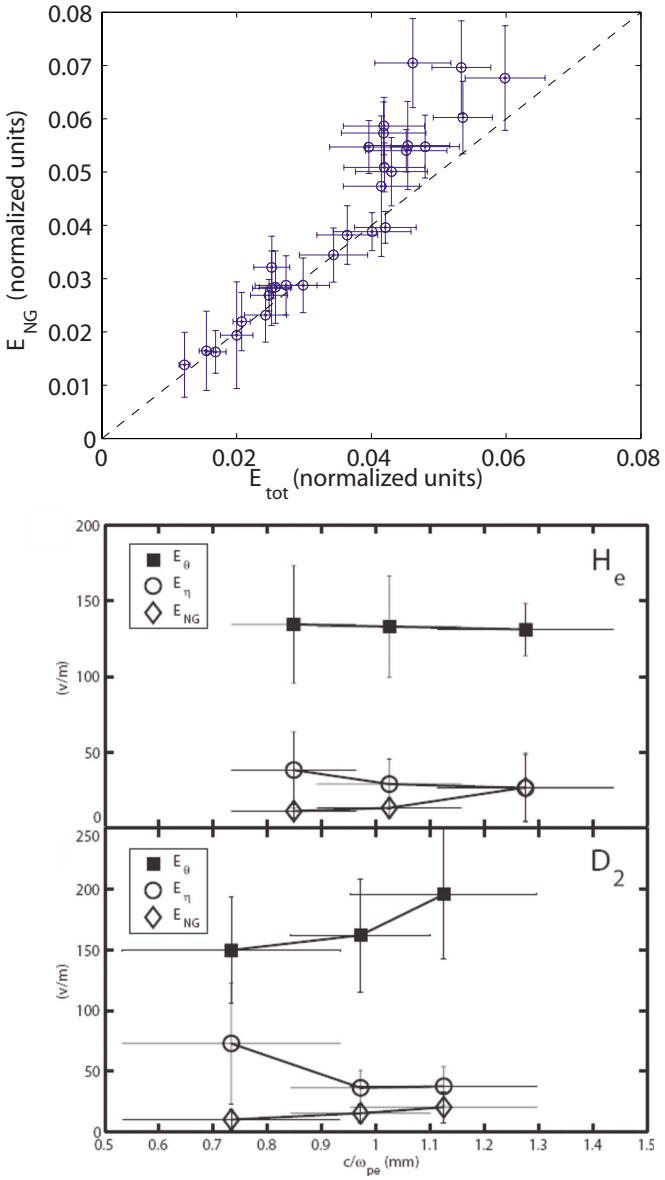

FIG. 14. (Color online) Balance of reconnection electric field near the X-point in the simulation (top) and experiment (reproduced from Ref. 3 by permission of American Geophysical Union) (bottom). Linear regime cases from Fig. 5 are shown; simulation data are averaged over $(0.5-0.7)\tau$; error bars represent the standard deviation from this averaging. In the experiment, E_θ is the reconnection electric field at the center of the layer, E_η is the portion of the field due to the classical Spitzer resistivity, and E_{NG} is the field estimated from Eq. (10). In the simulation, E_{NG} approximately balances the reconnecting electric field, but it is too small to do so in the experiment.

V. SUMMARY AND CONCLUSIONS

In order to model low collisionality regimes of operation of MRX, boundary conditions mimicking the experimental ones have been implemented in a fully kinetic 2D PIC code. The basic limitation of PIC codes, i.e., the need to resolve a large range of spatial and temporal scales, makes a simulation with realistic ion-to-electron mass ratio unfeasible. Thus, artificially low mass ratios were used and the geometry was scaled in such a way that characteristic scale lengths normalized to the ion skin depth in the simulation match those quantities in the experiment. Similarly, the characteristic time scale τ for the current ramp-down (the "drive time") was chosen in order to obtain the value of $\tau\Omega_{i0}$ similar to the one used in the experiments; this is accomplished by comparing features of the layer structure.

Using this scaling approach, overall dynamics resembling those observed in the experiments have been obtained. In particular, as the current in the flux cores is ramped down, a current sheet forms at the center of the device and subsequently evolves in a manner which allows for meaningful comparisons with experiments. The quadrupole structure of the magnetic field and appropriately normalized inflow/outflow velocity profiles are observed to well match the experimental ones. However, a detailed comparison of the electron layer structure between experiments and simulations revealed significant differences in the geometry of the electron diffusion region. For the simulations in this study, the thickness of the electron layer is in the range $\delta_{Bt} \approx (1.5-2)d_e$, which differs from the experimentally observed $\sim 8d_e$ by approximately a factor of 5. Over the range of $m_i/m_e = 10-150$ studied, the thickness in the simulation is observed to increase weakly with the mass ratio $\sim(m_i/m_e)^{1/6}$. Extrapolating to a realistic hydrogen mass ratio, this scaling implies a thickness $\delta_{Bt} \approx 3d_e$, which is still significantly less than the experimentally observed value.

The fine structure probes used to measure the electron layer in the experiment have a resolution up to 2.5 mm in the transverse direction across the layer. Since an electron skin depth is typically ~ 1 mm in the experiment, a layer thickness of a few skin depths should be resolved. However, current blockage due to the presence of the probes in the plasma may lead to a 6%–44% overestimate in the layer thickness depending on the ratio of the measured thickness to the glass tube radius.[3] Thus, instead of $\sim 8d_e$, the experimental thickness may be closer to $5.5d_e - 7.5d_e$, which is still significantly broader than the simulation by at least a factor of 3. Thus, we conclude that the layer is 3–5 times broader in the experiment than in the simulation; experimental resolution and probe effects are unlikely to be the source of the discrepancy.

A majority of 2D collisionless simulations report layer thicknesses of the order of a few d_e (which corresponds to the scale of the meandering orbits, as discussed in Sec. IV A). Thus, we are lead to conclude that effects excluded from 2D collisionless simulations, viz., 3D geometry and binary collisions, are responsible for the differences in the thickness of the layer. At the moment, it remains unclear whether this discrepancy also indicates that the physics of the reconnection electric field is different between the simulations and the experiments. Note that this possibility does not contradict the fact that the reconnection rate in the simulations matches well that in the experiments. Indeed, the linear scaling of the reconnecting electric field with the drive time (Fig. 5) indicates that for the simulations that are in the linear regime, the peak reconnection rate is set predominantly by the drive time. Thus, very different reconnection mechanisms may give similar reconnection rates. This in turn implies that the structure of the outer region may depend only weakly on the physics of the diffusion region.

Similar conclusions regarding the drive time have been drawn from previous simulations of driven magnetic reconnection[35] as well as plasma merging experiments in

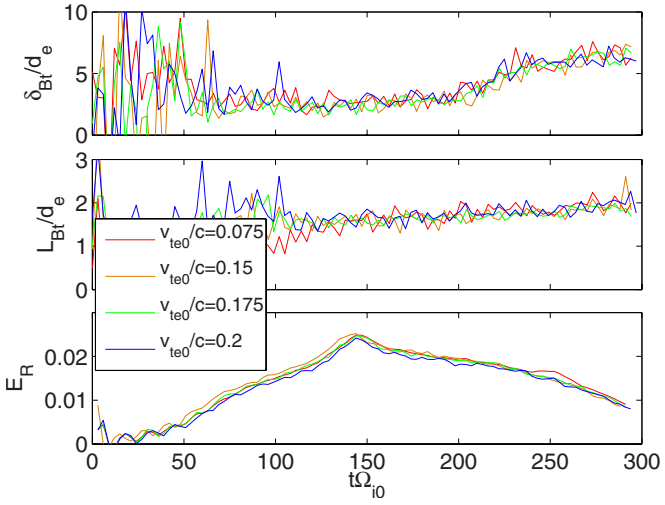

FIG. 15. (Color online) Scan of v_{te0}/c and ω_{pe}/Ω_{e0} with fixed $\beta_{e0}=0.059$. Other parameters are $m_i/m_e=25$, $\tau\Omega_{i0}=300$ $(\tau/\tau_{A0}=48.3)$, $n_0=1.25\times10^{13}$ cm^{-3}, and no reflection at the flux core surfaces.

TS-3.[36] In the latter case, two toroidal plasmas with either equal or opposite helicity were brought together to reconnect. While this experiment was carried out in collisional plasma, a similar linear dependence of the reconnection rate on the external forcing was observed.

As is mentioned above, collisions and/or effects associated with 3D geometry are likely to be responsible for the observed discrepancies. Although in MRX the layer thickness is an order of magnitude smaller than the electron mean free path, simple estimates show that the weak collisions present in MRX may significantly reduce the magnitude of the off-diagonal components of the electron pressure tensor. At the same time, a narrow current layer may be unstable to various current-aligned instabilities that are excluded from a 2D model. We note that electromagnetic fluctuations within the central region of the layer have been previously reported in MRX,[37] but a correlation with the thickness has not yet been established.

The resolution of the outstanding issues discussed in this paper will require both experimental and theoretical effort. In particular, a systematic analysis of the role of electromagnetic fluctuations in relation to the layer thickness and electron force balance in MRX is being performed. Similarly, work is underway to assess the role of binary collisions in simulations and eventually perform 3D simulations using the MRX geometry including binary collisions.

ACKNOWLEDGMENTS

This material is based on work supported by the National Science Foundation under Grant No. 0447423, by the Department of Energy Grant No. DE-FG02-06ER54893, and by NASA Grant No. NNG05GJ25G. S.D. was supported by a DOE Fusion Energy Sciences Fellowship and the NDSEG Fellowship Program. Simulations were partially performed at Los Alamos National Laboratory.

APPENDIX: FIXED BETA BENCHMARKING

As outlined in Sec. II B, an artificially high value of v_{te0}/c is used in the simulations in order to reduce the scale separation between the electron Debye length and skin depth. To explore the effect of this high electron temperature within the accessible parameter regime of the simulation, a scan of v_{te0}/c and ω_{pe0}/Ω_{e0} was performed with fixed $\beta_{e0}=0.059$. Figure 15 demonstrates that the scaling results for the length and width of the layer as well as the reconnection rate E_R are not affected by this parameter scan, especially during the time period from $t\Omega_{i0}=0.5\tau=150$ onwards, where data are typically measured. This means that the results in this work should not be sensitive to the choice of a high v_{te0}/c since β_{e0} is in the correct range for MRX.

[1] D. A. Uzdensky and R. M. Kulsrud, Phys. Plasmas **13**, 062305 (2006).
[2] W. Daughton, J. Scudder, and H. Karimabadi, Phys. Plasmas **13**, 072101 (2006).
[3] H. Ji, Y. Ren, M. Yamada, S. Dorfman, W. Daughton, and S. Gerhardt, Geophys. Res. Lett. **35**, L13106, DOI: 10.1029/2008GL034538 (2008).
[4] M. Ugai and T. Tsuda, J. Plasma Phys. **17**, 337 (1977).
[5] D. Biskamp, Phys. Fluids **29**, 1520 (1986).
[6] D. Uzdensky and R. Kulsrud, Phys. Plasmas **7**, 4018 (2000).
[7] M. Hesse, K. Schindler, J. Birn, and M. Kuznetsova, Phys. Plasmas **6**, 1781 (1999).
[8] M. Shay, J. Drake, B. Rogers, and R. Denton, J. Geophys. Res. **106**, 3759, DOI: 10.1029/1999JA001007 (2001).
[9] H. Karimabadi, W. Daughton, and J. Scudder, Geophys. Res. Lett. **34**, L13104, DOI: 10.1029/2007GL030306 (2007).
[10] M. Shay, J. Drake, and M. Swisdak, Phys. Rev. Lett. **99**, 155002 (2007).
[11] T. Phan, J. Drake, M. Shay, F. Mozer, and J. Eastwood, Phys. Rev. Lett. **99**, 255002 (2007).
[12] B. Rogers, R. Denton, J. Drake, and M. Shay, Phys. Rev. Lett. **87**, 195004 (2001).
[13] M. Shay, J. Drake, and M. Swisdak, Phys. Plasmas **11**, 2199 (2004).
[14] L. Chacón, A. N. Simakov, and Z. Zocco, Phys. Rev. Lett. **99**, 235001 (2007).
[15] J. Wygant, J. Geophys. Res. **110**, A09206, DOI: 10.1029/2004JA010708 (2005).
[16] F. S. Mozer, S. D. Bale, J. P. McFadden, and R. B. Torbert, Geophys. Res. Lett. **32**, 24102, DOI: 10.1029/2005GL024092 (2005).
[17] Y. Ren, M. Yamada, H. Ji, S. Dorfman, S. Gerhardt, and R. Kulsrud, Phys. Plasmas **15**, 082113 (2008).
[18] Y. Ren, M. Yamada, H. Ji, S. P. Gerhardt, and R. Kulsrud, Phys. Rev. Lett. **101**, 085003 (2008).
[19] V. Vasyliunas, Rev. Geophys. **13**, 303, DOI: 10.1029/RG013i001p00303 (1975).
[20] J. W. Dungey, in *Reconnection in Space Plasma* (European Space Agency, Paris, 1989), pp. 15–19.
[21] L. R. Lyons and D. C. Pridmore-Brown, J. Geophys. Res. **95**, 20903, DOI: 10.1029/JA095iA12p20903 (1990).
[22] P. Pritchett, J. Geophys. Res. **106**, 3783, DOI: 10.1029/1999JA001006 (2001).
[23] M. M. Kuznetsova, M. Hesse, and D. Winske0, J. Geophys. Res. **106**, 3799DOI: 10.1029/1999JA001003 (2001).
[24] M. Hesse, J. Birn, and M. Kuznetsova, J. Geophys. Res. **106**, 3721, DOI: 10.1029/1999JA001002 (2001).
[25] M. Yamada, H. Ji, S. Hsu, T. Carter, R. Kulsrud, N. Bretz, F. Jobes, Y. Ono, and F. Perkins, Phys. Plasmas **4**, 1936 (1997).
[26] Y. Ren, M. Yamada, S. Gerhardt, H. Ji, R. Kulsrud, and A. Kuritsyn, Phys. Rev. Lett. **95**, 055003 (2005).
[27] M. Yamada, Y. Ren, H. Ji, J. Breslau, S. Gerhardt, R. Kulsrud, and A. Kuritsyn, Phys. Plasmas **13**, 052119 (2006).
[28] N. A. Murphy and C. R. Sovinec, Phys. Plasmas **15**, 042313 (2008).
[29] A. Kuritsyn, H. Ji, S. Gerhardt, Y. Ren, and M. Yamada, Geophys. Res. Lett. **34**, L16106, DOI: 10.1029/2007GL030796 (2007).
[30] W. Daughton, Phys. Plasmas **10**, 3103 (2003).
[31] W. Daughton and P. Ricci, Phys. Rev. Lett. **93**, 105004 (2004).
[32] R. Morse and C. Nielson, Phys. Fluids **14**, 830 (1971).
[33] D. Forslund, Space Sci. Rev. **42**, 3 (1985).

[34]M. Kuznetsova, M. Hesse, and D. Winske, J. Geophys. Res. **103**, 199, DOI: 10.1029/97JA02699 (1998).
[35]J. Birn and M. Hesse, Phys. Plasmas **14**, 082306 (2007).
[36]M. Yamada, Y. Ono, A. Hayakawa, M. Katsurai, and F. Perkins, Phys. Rev. Lett. **65**, 721 (1990).
[37]H. Ji, S. Terry, M. Yamada, R. Kulsrud, A. Kuitsyn, and Y. Ren, Phys. Rev. Lett. **92**, 115001 (2004).
[38]See EPAPS Document No. E-PHPAEN-15-024810 for movies showing the time evolution. For more information on EPAPS, see http://www.aip.org/pubservs/epaps.html.

The Princeton Plasma Physics Laboratory is operated
by Princeton University under contract
with the U.S. Department of Energy.

Information Services
Princeton Plasma Physics Laboratory
P.O. Box 451
Princeton, NJ 08543

Phone: 609-243-2750
Fax: 609-243-2751
e-mail: pppl_info@pppl.gov
Internet Address: http://www.pppl.gov